J. Synchrotron Rad. (1998). **5**, 232–238

Instrumentation Developments for X-ray Linear and Circular Dichroism at the ESRF Beamline ID12A

José Goulon,[a]* Andrei Rogalev,[a] Christophe Gauthier,[a] Chantal Goulon-Ginet,[b] Stéphane Paste,[a] Riccardo Signorato,[a] Claus Neumann,[a] Laurence Varga[c] and Cécile Malgrange[c]

[a]European Synchrotron Radiation Facility, BP 220, F-38043 Grenoble, France, [b]Faculté de Pharmacie, Université Joseph Fourier, BP 53, F-38041 Grenoble, France, and [c]Laboratoire de Minéralogie Cristallographie, Universités Paris 6 and Paris 7, 4 Place Jussieu, Case 115, F-75252 Paris CEDEX 05, France. E-mail: goulon@esrf.fr

(*Received 4 August 1997; accepted 20 October 1997*)

This paper reports on the performance of the instrumentation developed for the ESRF beamline ID12A, which is dedicated to spectroscopic applications requiring full control of the polarization at energies $\geq$2.0 keV. Emphasis is placed on the characterization of various optical components of the beamline and on problems associated with either the control or the conversion of the polarization state. A few examples have been selected to illustrate what sort of new spectroscopic information has already been obtained at the beamline. These include the comparison of X-ray magnetic dichroism spectra recorded with linear or circular polarization and the very first detection of X-ray natural circular dichroism in single crystals known to exhibit a very large non-linear susceptibility at optical wavelengths.

Keywords: X-ray magnetic circular dichroism (X-MCD); X-ray magnetic linear dichroism (X-MLD); X-ray natural circular dichroism (X-NCD); X-ray polarimetry.

1. Introduction

Two helical undulators (Helios-I and Helios-II) have been inserted into the ID12 high-β straight section of the ESRF storage ring. These powerful X-ray sources are shared by two beamlines, which are both optimized for spectroscopic applications requiring the control of the polarization of the incident radiation over a wide energy range extending from $\sim$0.4 to 20 keV. The two beamlines complement each other because of the different nature of their optics:

(i) Dynamical diffraction by perfect crystals used either as monochromators or polarizers is the approach retained for beamline ID12A, which is dedicated to experiments carried out at energies $\geq$2 keV.

(ii) The low-energy side-branch ID12B is equipped with a 'Dragon' spectrometer which couples Kirkpatrick–Baez refocusing optics to an SEM grating monochromator (Chen, 1987; Chen & Sette, 1989).

The present paper deals with instrumentation and technical developments specific to beamline ID12A. Since there are related papers reviewing the design of helical undulators (Chavanne *et al.*, 1998) or addressing the key problem of wide-band X-ray absorption spectroscopy or dichroism using the 'gap-scan' technique (Rogalev *et al.*, 1998) in the same issue, we will lay emphasis here on the status and performances of the main optical components of the beamline. We will also report briefly on the use of quarter-wave plates with circularly polarized X-ray beams: we started with the experimental determinations of the Poincaré–Stokes components either upstream or downstream with respect to the Bragg monochromator (Goulon *et al.*, 1996; Varga *et al.*, 1997) and are now concentrating on linear-dichroism experiments with the attractive advantage that the polarization vector can be freely rotated around the beam-propagation direction. In the final section of the paper we have selected a pair of test experiments which illustrate the quality of the data collected on beamline ID12A and show that this beamline can give access to new spectroscopic information: particularly noteworthy is the first experimental observation of X-ray natural circular dichroism (X-NCD) in single crystals known to exhibit a large non-linear electrical susceptibility at optical wavelengths.

2. Beamline instrumentation

2.1. *Beamline general concept*

Over the past three years the two beamlines ID12A and ID12B have been operated full-time in parallel for the greatest benefit of the ESRF users. What appears trivial now was not taken for granted in the early stages of the project and we wish to stress here the conditions which made the parallel operation possible. The first condition concerns the source design. Even though Helios-I and

Helios-II are based on the same basic concept (Elleaume, 1994), there are noticeable differences between them:

(i) Helios-II has a shorter magnetic period ($\lambda_u = 52$ mm) than Helios-I ($\lambda_u = 85$ mm) so that the two insertion devices span different (overlapping) spectral ranges: with a fundamental emission peaking at $E \geq 2.1$ keV, Helios-II is ideally suited for beamline ID12A.

(ii) Helios-I is made of two segments which, by construction, generate two X-ray beams of opposite helicity: a magnetic chicane causes each segment to emit slightly off-axis, *i.e.* at an angle $\pm\Delta\theta$ with respect to the direction of emission of Helios-II.

Even though the 'kick' angle $2\Delta\theta$ is as small as 200–360 µrad, this is large enough to have three beams (*i.e.* Helios-IA, Helios-II and Helios-IB) fully separated at the beamline front end, *i.e.* at 26.5 m from the middle point of Helios-I. It can be seen from the beamline layout reproduced in Fig. 1 that the first component (common to beamlines ID12A and ID12B) is a 'multi-pinhole' device designed to accommodate three beams, with the further complication that the angular divergence of Helios-IA and Helios-IB increases on closing the undulator half-gaps. This device (Brookes, 1994) consists of two copper plates which can be translated vertically with respect to each other: the first plate combines a V-shaped groove (to pass Helios-IA and Helios-IB) plus a vertical groove that coincides with the axis of symmetry of the V (to allow the central beam of Helios-II to pass through); the second plate has a variety of horizontal slots to optionally select one, two or three beams.

As illustrated by Fig. 2, the most common way to activate the side-branch beamline ID12B is by inserting two mirrors (*i.e.* DFM-IA and DFM-IB) that intercept the two beams of Helios-I (*i.e.* Helios-IA and Helios-IB) and deflect them at 4° in the horizontal plane. What makes possible a parallel operation of beamlines ID12A and ID12B is a 3 mm-diameter hole channelling along the mirror DFM-IB so that the central beam of Helios-II is not stopped. Given the low figure slope error ($\leq$0.5 arcsec) specified for the DFM mirrors of the Dragon beamline, the additional request to have such a hole very near the reflective surface of mirror DFM-IB was a risky challenge met successfully by the polishing company SESO Inc. (France): during the optical qualification tests of mirror DFM-IB, we failed to detect any local defect induced by the hole. This may be due to the remarkable stiffness of CVD-SiC which was selected as the substrate material for all mirrors of beamlines ID12A and ID12B. Unless there is some request from the users for a very exotic mode of operation, we do not need to readjust the pinhole device nor the mirror DFM-IB over periods as long as six months; this is a positive indication of the global stability of the ESRF source.

What is lost in the parallel operation of beamlines ID12A and ID12B is the capability for the users of beamline ID12A to flip rapidly the photon helicity, as this is possible only with the two beams of Helios-I. This stimulated the development of a new type of electromagnetic undulator to restore such 'fast-switching' capability (Chavanne *et al.*, 1998).

2.2. *Horizontally deflecting four-mirror device*

In the layout shown in Fig. 1, the first optical component specific to beamline ID12A is the four-mirror device,

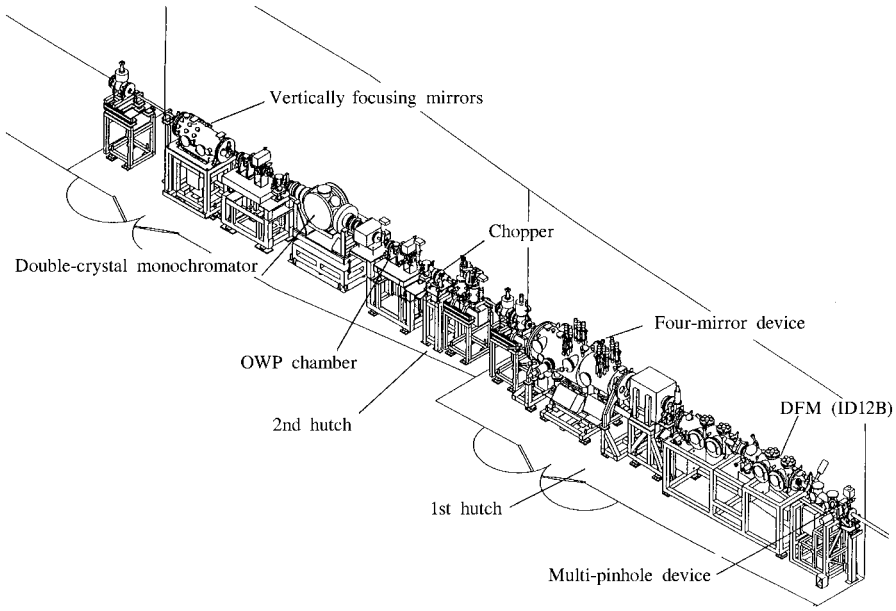

Figure 1
Layout of the ESRF beamline ID12A optical hutches. Clearly identified components are the multi-pinhole device, the deflecting mirrors, DFMs, used to activate beamline ID12B, the horizontally deflecting four-mirror device, the secondary slits, the double-crystal monochromator, the vertically focusing double-mirror device (VF-2M) and one of the various beam-position monitors available along the beamline.

which has three major functions (Pasté *et al.*, 1993; Pasté, 1997):

(i) It is used primarily as a very efficient energy low-pass filter to eliminate unwanted harmonics and minimize the heat load on the monochromator.

(ii) It can be used to steer independently two beams in the horizontal plane (*e.g.* Helios-IA and Helios-IB or Helios-II and Helios-IB) and let them hit the sample on a single spot. This is crucial for dichroism experiments whenever the sample has heterogeneous domains.

(iii) It has the capability to refocus the two beams in the horizontal plane under the restriction that the monochromator located downstream is diffracting in the vertical plane so that we do not spoil the excellent energy resolution.

For each beam, a double reflection on two mirrors set in an antiparallel $(+, -)$ configuration is ideal to fulfil the above requirements. The complexity of the mechanical design, illustrated by Fig. 3, stems from geometrical constraints due to the proximity of the two beams and from the requirement to operate reliably the whole optical system under clean UHV conditions ($\leq 5 \times 10^{-9}$ mbar). Interventions in the 'optics hutch' have to be kept very rare since both beamlines, *i.e.* ID12A and ID12B, have to be shut down. Each mirror has three motorized degrees of freedom:

(*a*) a lateral translation T_x (≤ 7 mm, resolution 0.08 μm step^{-1}) used to intercept the beam;

(*b*) two (small-amplitude) rotations using flexure hinges: $R_z \leq 30$ mrad (resolution ≤ 0.15 μrad step^{-1}, for mirrors 1*A*, 1*B*) required to vary the angle of incidence; $R_s \leq \pm 100$ μrad (resolution 5 μrad step^{-1}) required to set the reflecting planes strictly vertical.

Two additional translations are also available:

(*a*) a vertical translation of the whole mirror assembly T_z (≤ 20 mm; resolution 1.2 μm step^{-1}) makes it possible to align properly the whole device but also to select the desired reflecting strip (*e.g.* bare SiC surface or Cr layer);

(*b*) a long-stroke axial translation T_s (≤ 600 mm; resolution 2.5 μm step^{-1}) of the second pair of mirrors (2*A*, 2*B*) is to be used only when the mirrors are operated at very grazing incidences.

As is apparent from Fig. 3, a diamond-like shape was given to the first mirrors (1*A*, 1*B*) so that three-point bender mechanics makes it easy to induce a small curvature ($R \geq 700$ m), while the second mirrors (2*A*, 2*B*) always remain flat. Given the nature of the substrate (CVD-SiC) and the rather large size of the mirror plates ($600 \times 40 \times 12$ mm), we had to accept less stringent polishing specifications regarding the figure accuracy: the latter was still kept better than 0.8 arcsec for flat surfaces featuring a residual curvature ≥ 14 km. With a surface

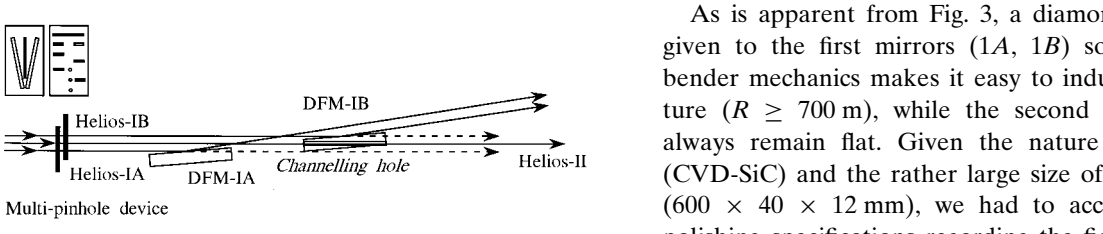

Figure 2
Three-beam geometry for parallel operation of beamline ID12A and ID12B (top view).

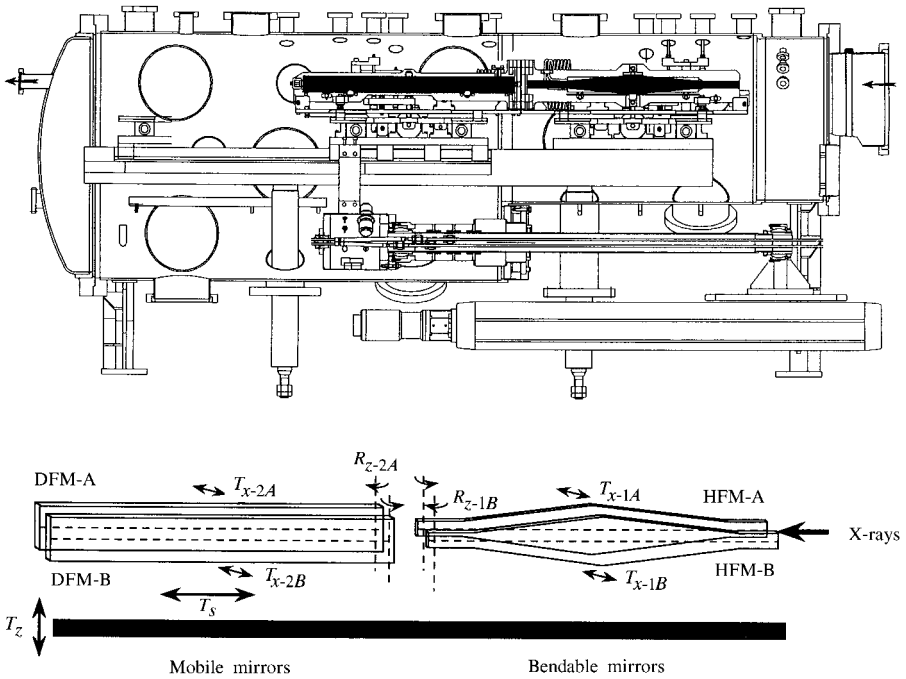

Figure 3
Schematic side views of the four-mirror device in its vacuum vessel. The lower sketch was added to show explicitly the various mechanical degrees of freedom of the instrument.

microroughness $\leq$5 Å r.m.s., the transmitted intensity after two reflections on bare SiC surfaces was found to be of the order of 67% at 3 keV for 8 mrad incidence. On the other hand, optical metrology tests carried out on these mirrors revealed structured slope errors of low spatial periodicity ($\leq L/2$) with detrended errors in excess of 600 nm: this is large enough to induce at very grazing incidences some hardly controllable horizontal refocusing without acting the mirror bender. Another difficulty concerned dramatic figure distortions caused by the heat exchangers improperly located on the back of the mirrors: more specifically, the gallium layer added to improve the thermal contact was found to create undesirable surface tensions and, finally, had to be removed. Nevertheless, as illustrated by Fig. 4(*a*), refocusing in the horizontal plane turned out to be feasible and a typical beam size of the order of 350 µm (FWHM) is currently used.

Regarding the harmonic suppression, numerous tests have been performed (Pasté, 1997) either on using energy-resolved solid-state detectors in combination with absorbing foils or, more reliably, on scanning the monochromator beyond the energy cut-off of the four-mirror device. At 5 mrad incidence, with the fundamental of the undulator peaking at 4 keV, the intensity of the second harmonics was found to decrease by three orders of magnitude. Similarly, we observed that the level of the third harmonics did not exceed a few p.p.m.

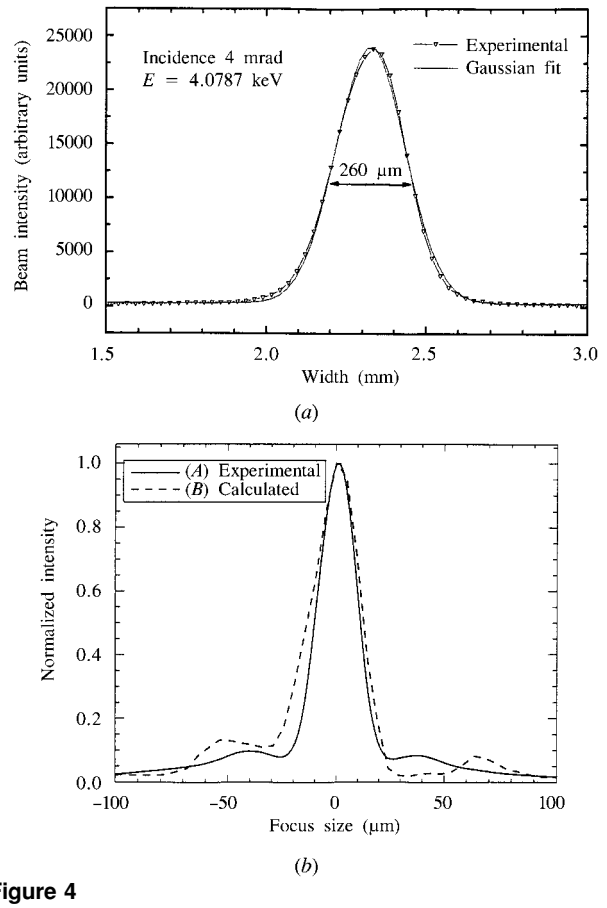

Figure 4
Beam intensity distributions along the (*a*) horizontal axis and (*b*) vertical axis. (*a*) Source-to-image distance 41.2 m; source-to-HFM1 distance 31.2 m; incidence 4 mrad. The smooth Gaussian profile results from the convolution with a broad source. (*b*) Source-to-focus distance 50.8 m; source-to-VFM1 distance 42.8 m; incidence 5 mrad. Note the presence of satellites characteristic of structured slope errors.

2.3. *Refocusing optics in the vertical plane*

A double-mirror device (VF-2M) located just before the beam shutter of the second hutch, *i.e.* downstream with respect to the monochromator, and after the first experimental station, operates with the monochromatic beam. The primary function of the VF-2M device is to refocus the beam in the vertical plane very near the sample location, *i.e.* with a significant demagnification factor. Indeed, it can act as a further low-pass filter just as efficient as the four-mirror device. The system (Fig. 5) combines two identical mirrors (600 × 40 × 12 mm) polished to a cylindrical shape with a concave curvature of 1 km with a figure accuracy $\leq$0.8 arcsec and a surface microroughness of 2.5 Å r.m.s. A mechanical four-point bender makes it possible to vary continuously the curvature radius from 1 km concave to 1 km convex (Signorato *et al.*, 1996, 1997). Key components in this design are UHV-compatible self-compensated piezoactuators with nanometric resolution from Queensgate Instruments Ltd (UK). It was checked (Signorato *et al.*, 1996) that the antiparallel (+, −) configuration is almost self-compensating with respect to the gravity sag. As illustrated by Fig. 4(*b*), vertical focus sizes as small as 22 µm (FWHM) have been obtained while keeping all vertical slits fully open. Geometrical aberrations do not yet limit the performances: as discussed elsewhere (Signorato & Sanchez del Rio, 1997), careful optical metrology tests have again revealed structured slope errors with characteristic periodicity between 1/2 and 1/20 of the mirror length, which affect the shape of the

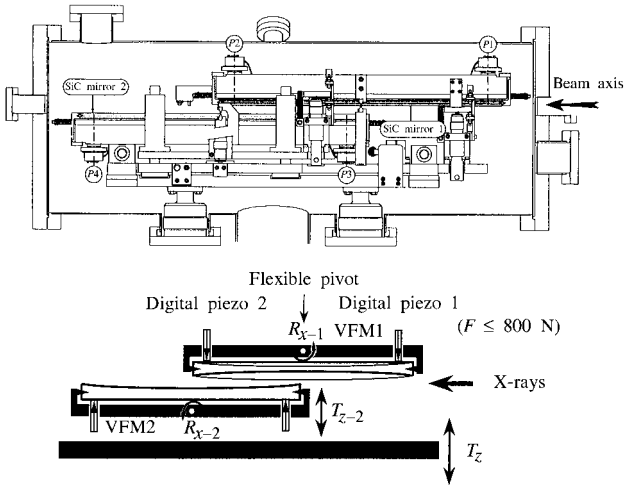

Figure 5
Schematic side views of the vertically refocusing double-mirror device in its vacuum vessel. The lower sketch was again added to show clearly the main mechanical degrees of freedom of the instrument.

focal spot, its size and position but also generate satellite structures, apparent in Fig. 4(*b*). Since it may be difficult to improve further the polishing techniques at reasonable cost, a possible strategy to remove such undesirable effects is to use segmented bimorph mirrors with adaptive correctors, as reported elsewhere in this issue (Signorato *et al.*, 1998).

2.4. *Double-crystal monochromator*

The fixed-exit two-crystal monochromator of beamline ID12A was manufactured for the ESRF by KoHzu Seiki Co. (Japan). It is an upgraded UHV-compatible version of the single- or double-cam monochromators introduced ten years ago (Goulon *et al.*, 1983; Matsushita *et al.*, 1986). The uncommon implementation of an axial rotation R_s ($\pm 48^\circ$) of the whole instrument around the direction of the incident beam proved to be essential for some linear dichroism or polarimetry experiments at Bragg angles approaching 45°, but turned out to be also very convenient for refined alignments (see Appendix *A* of Goulon *et al.*, 1996). The temperature of each individual crystal can be stabilized to ± 0.2 K at any desired temperature from room temperature down to 140 K by circulating refrigerated He gas in a closed circuit. Time and effort have been invested in developing in-house our own cryogenic cooling system, which proved to be completely vibration free. Typically, with a pair of Si(111) crystals, the stability of the maximum of the rocking curve after several XAFS scans was found to be better than 0.14 arcsec over periods of several hours.

2.5. *Polarimetry studies*

A major concern in circular dichroism experiments is the determination of the circular-polarization rate of the monochromatic beam, which depends not only on the polarization of the undulator radiation but also on the polarization transfer functions or Mueller matrices of all optical components including the monochromator (Malgrange *et al.*, 1991). It is therefore desirable to insert at several places along the beamline UHV-compatible X-ray polarimeters, which consist of a quarter-wave plate plus a linear analyzer. X-ray phase plates exploit the birefringence of perfect crystals under the conditions of Bragg diffraction (Molière, 1939) and the most convenient option consists of using the forward-diffracted beam outside the range of total reflection since the transmitted beam is not deviated (Hirano *et al.*, 1991, 1992). The phase shift φ between the σ and π components of the polarization vector is given by

$$\varphi = -(\pi/2)\, Az/\Delta\theta \cos\psi, \qquad (1)$$

where z is the crystal thickness, ψ is the angle between the incident-beam wavevector and the normal to the crystal surface, $\Delta\theta$ is the angular offset (defined as the difference between the true angle of incidence θ and the Bragg angle θ_0 at the middle of the reflection profile) and A is a factor that depends on energy and on the nature of the crystal. For $\varphi = \pi/2$, a circular polarization is transformed into a linear polarization but the σ and π components may not be attenuated in the same proportions so that the polarization vector is rotated (with respect to the plane of diffraction of the phase plate) by the angle $\alpha \neq 45^\circ$ satisfying the condition: $\tan\alpha = (I_\sigma/I_\pi)^{1/2}$ (Goulon *et al.*, 1996; Varga *et al.*, 1997). Owing to the necessity to minimize the absorption losses, diamond crystals are usually preferred for experiments above 3 keV even though ultra-thin silicon crystals have been successfully used at energies as low as 2.8 keV (Goulon *et al.*, 1996). On the other hand, X-ray linear analyzers most often use the property that only the polarization component perpendicular to the scattering plane can be scattered at 90°: either coherent scattering (*i.e.* Bragg diffraction at 45°) or incoherent scattering can be used.

We have designed a standard UHV-compatible polarimeter chamber in which we can insert either a phase plate or a linear analyzer. A major feature of the chamber, which looks like a six-way cross, is that it can be rotated around the beam axis thanks to a high-precision playless helical wormscrew (Zahnradfabrik OTT, Germany), whereas a differentially pumped rotary drive (DRF-55 from VG-Instruments, UK) is used to generate a rotation around any axis perpendicular to the beam direction (Goulon *et al.*, 1996). Three chambers of this type are permanently inserted into the beamline, *i.e.* one for every experimental station. This resulted in the possibility of measuring the polarization state of the incident radiation either before or after the monochromator. The main difficulty experienced with this set-up is the alignment of the rotation axis of the polarimeter chambers parallel to the beam direction, especially when the four-mirror device is used. As far as one is interested only in the circular-polarization rate (Poincaré–Stokes parameter P_3), one can remove this difficulty by recording and fitting the intensity profiles $I_s(\theta)$ measured by the analyzer on scanning the offset of the quarter-wave plate across the Bragg reflection (Varga *et al.*, 1997).

While the polarization rate measured upstream with respect to the monochromator with a single beam of Helios-I was excellent ($P_3 \geq 97\%$), more recent measurements carried out during the parallel operation of beamlines ID12A and ID12B have revealed a significant level of depolarization of the central beam (Helios-II), with circular polarization rates of only $P_3 \simeq 90\%$ on using the second harmonic of the undulator. We suspect that the central beam may, unfortunately, be slightly contaminated by the adjacent beams Helios-IA and Helios-IB, which feature opposite polarization and may contribute to some depolarized background. Supporting our interpretation is the observation, illustrated by Fig. 6, that the intensity profiles $I_s(\theta)$, measured with a phase plate located downstream with respect to the monochromator and supposed to intercept only the Helios-II beam, were quite sensitive to changes in the half-gaps (phase) of Helios-I. Even though the perturbation looks particularly dramatic on

closing the half-gaps of Helios-I, the corresponding change in the circular polarization rate P_3 is $\leq 10\%$, whereas reversing the phase of Helios-I does not alter P_3 by more than 1–2%. Nevertheless, the reality of such undesired cross-talk effects between beamlines ID12A and ID12B call for a comprehensive interaction between the users of both beamlines.

3. Spectroscopic applications

In this last section we would like to illustrate the performances of the beamline using some recent experiments carried out as part of the in-house research program at beamline ID12A.

3.1. *Comparison of X-MCD and X-MLD spectra*

As described in §2.5, a crystal plate will convert circularly polarized radiation into linearly polarized radiation if the phase shift is $\pm\pi/2$. Furthermore, the orientation of the polarization vector can be freely selected by rotating the diffraction plane (or the unit vector normal to the phase plate) around the beam direction, *i.e.* by rotating the polarimeter chamber around the beam axis. This is a fairly substantial advantage for polarization-dependent XAFS studies on single crystals or anisotropic systems since we no longer need to rotate the sample, which often turns out to be a serious handicap if the sample is inserted inside a photoemission chamber, a bulky cryostat or inside the poles of a heavy magnet. It should also be kept in mind that rotating a single crystal may reveal glitches or generate more subtle artefacts when one is looking at the angular dependence of X-ray absorption spectra either in the transmission or in the fluorescence yield modes (Brouder, 1990). As far as linear dichroism studies are concerned, one is merely interested in measuring directly difference absorption cross sections for orthogonal orientations of the polarization vector; instead of rotating the polarimeter chamber by 90° (which is implicitly a slow

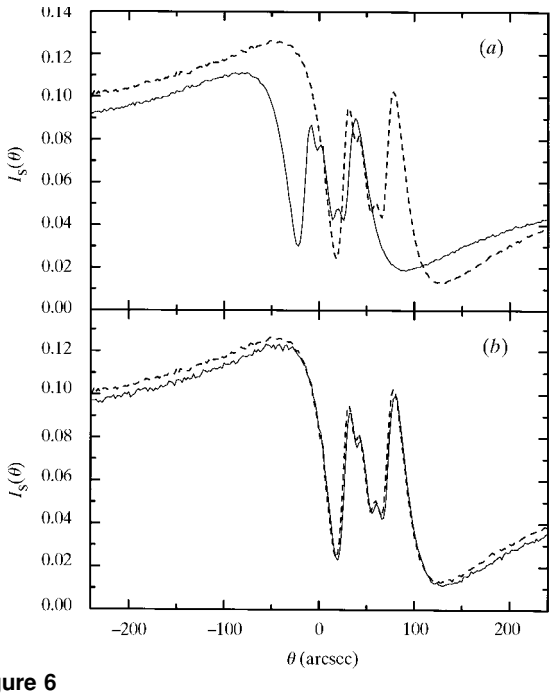

Figure 6
Perturbations caused to the transmission intensity profiles of a diamond phase plate inserted in beamline ID12A downstream with respect to the monochromator when users of beamline ID12B (*a*) open/close the gaps of Helios-I or (*b*) reverse its phase. Dramatic effects (up to 10% change in P_3) were observed only for large changes of gaps.

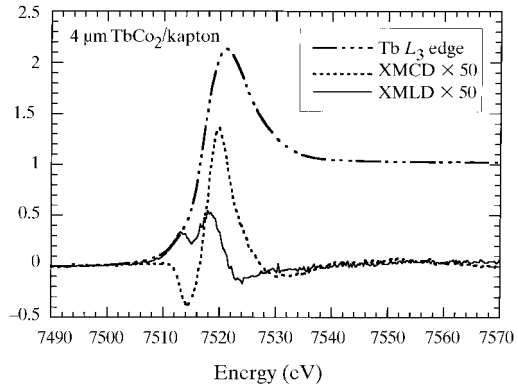

Figure 7
Comparison of X-MLD and X-MCD spectra recorded in transmission on amorphous $TbCo_2$ Laves phases at 25 K. A transverse (axial) magnetic field of 5 T was used for the X-MLD (X-MCD) experiment.

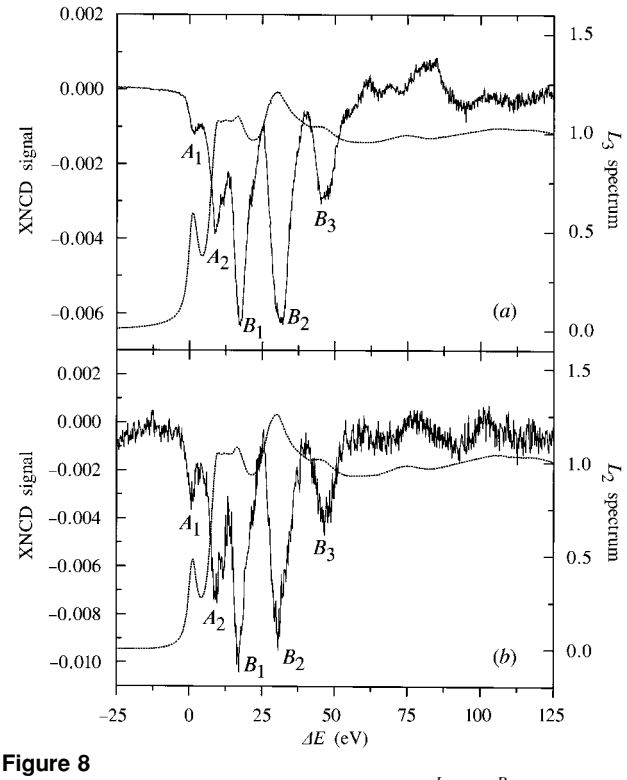

Figure 8
Normalized X-NCD spectral differences ($\sigma^L - \sigma^R$) recorded at the iodine (*a*) L_{III}-edge and (*b*) L_{II}-edge using an α-$LiIO_3$ single crystal aligned so that the optical axis was collinear with the incident X-ray beam. The polarization-averaged XANES spectra are also displayed for reference. Note the striking similarity in the morphology of the two X-NCD spectra which have the same sign.

motion!), it is, by far, much more attractive to invert the angular offset $\Delta\theta$, since this is associated with a very small angular change which can be performed very quickly using a flexure hinge system driven by a digital piezoactuator from Queensgate Instruments Ltd (Goulon *et al.*, 1996). In this way it becomes feasible to rotate the polarization vector by 90° several times for each data point of an XANES or EXAFS scan; the experiments become inherently much less sensitive to low-frequency source instabilities or drifts so that tiny (magnetic or natural) linear dichroism signals can now be measured accurately.

In order to illustrate the potentiality of this technique, we have reproduced in Fig. 7 the Tb L_{III}-edge X-MLD and X-MCD spectra recorded in the transmission mode on amorphous $TbCo_2$ Laves phases cooled to 25 K. A transverse (axial) magnetic field of 5 T was used for the X-MLD (X-MCD) study. This comparison clearly shows that the two experiments yield complementary information, especially in the energy range where the electric quadrupole terms $E2$ are expected to contribute. Even though the X-MLD signal is smaller than the X-MCD signal, the signal-to-noise ratio obtained in just a few test scans is excellent. More work is in progress to refine the corresponding data analyses (Varga *et al.*, 1998).

3.2. *X-ray natural circular dichroism in gyrotropic crystals*

We have recently produced the very first experimental evidence of X-NCD in a uniaxial gyrotropic single crystal of α-$LiIO_3$ which is currently used to frequency-double a number of lasers (Goulon *et al.*, 1998). We have reproduced in Fig. 8 the nicely structured difference spectra ($\sigma^L - \sigma^R$) recorded at the L_{II-III} edges of iodine using the fluorescence yield technique. Since the crystal optical axis was set collinear to the direction of the exciting X-ray beam, we did not worry about undesirable birefringence and linear dichroism effects. Note that the X-NCD spectra measured at the L_{II} and L_{III} edges are very similar and have the same sign. This is in contrast with X-MCD spectra which classically exhibit opposite signs at the L_{II} and L_{III} edges: while spin-orbit interaction is the driving term in X-MCD, the X-NCD signatures have to be assigned to the electric-dipole–electric-quadrupole ($E1E2$) terms which do not vanish in gyrotropic crystals but contribute to a crystal field-induced second-order polarizability. The latter interpretation is fully consistent with band-structure calculations (Goulon *et al.*, 1998) and with multiple scattering calculations (Natoli *et al.*, 1998).

References

Brookes, N. B. (1994). *Application Note on the Multi-pinhole Device*. ESRF internal document, pp. 1–5. ESRF, Grenoble, France.

Brouder, C. (1990). *J. Phys. Condens. Matter*, **2**, 701–738.

Chavanne, J., Elleaume, P. & Van Vaerenbergh, P. (1998). *J. Synchrotron Rad.* **5**, 196–201.

Chen, C. T. (1987). *Nucl. Instrum. Methods*, A**256**, 595–604.

Chen, C. T. & Sette, F. (1989). *Rev. Sci. Instrum.* **60**, 1616–1621.

Elleaume, P. (1994). *J. Synchrotron Rad.* **1**, 19–26.

Goulon, J., Goulon-Ginet, C., Rogalev, A., Gotte, V., Malgrange, C. & Brouder, C. (1998). *J. Chem. Phys.* Submitted.

Goulon, J., Lemonnier, M., Cortès, R., Retournard, A. & Raoux, D. (1983). *Nucl. Instrum. Methods*, A**208**, 625–630.

Goulon, J., Malgrange, C., Giles, C., Neumann, C., Rogalev, A., Moguiline, E., De Bergevin, F. & Vettier, C. (1996). *J. Synchrotron Rad.* **3**, 272–281.

Hirano, K., Izumi, K., Ishikawa, T., Annaka, S. & Kikuta, S. (1991). *Jpn. J. Appl. Phys. Lett.* **30**, L407–L410.

Hirano, K., Kanzaki, K., Mikami, M., Miura, M., Tamasaku, K., Ishikawa, T., Annaka, S. & Kikuta, S. (1992). *J. Appl. Cryst.* **25**, 531–535.

Malgrange, C., Carvalho, C., Braicovich, L. & Goulon, J. (1991). *Nucl. Instrum. Methods*, A**308**, 390–396.

Matsushita, T., Ishikawa, T. & Oyanagi, H. (1986). *Nucl. Instrum. Methods*, A**246**, 377–386.

Molière, G. (1939). *Ann. Phys.* **3**, 272–313.

Natoli, C. R., Brouder, C., Sainctavit, Ph., Goulon, J., Goulon-Ginet, C. & Rogalev, A. (1998). *Eur. Phys. J.* Submitted.

Pasté, S. (1997). PhD thesis, Université de Paris VI, France.

Pasté, S., Emerich, H., Goulon-Ginet, C. & Goulon, J. (1993). *Application Note on the Operation of the Four-Mirror Device*. ESRF internal document, pp. 1–31. ESRF, Grenoble, France.

Rogalev, A., Gotte, V., Goulon, J., Gauthier, C., Chavanne, J. & Elleaume, P. (1998). *J. Synchrotron Rad.* **5**, 989–991.

Signorato, R., Goulon-Ginet, C., Goulon, J. & Rogalev, A. (1996). *SPIE*, **2856**, 343–354.

Signorato, R., Goulon-Ginet, C., Goulon, J., Rogalev, A., Marion, P. & Fermé, J. J. (1997). *J. Phys. IV*, **7**(C2), 341–342.

Signorato, R., Hignette, O. & Goulon, J. (1998). *J. Synchrotron Rad.* **5**, 797–800.

Signorato, R. & Sanchez del Rio, M. (1997). *SPIE J.* **3152**. In the press.

Varga, L., Giles, C., Neumann, C., Rogalev, A., Malgrange, C., Goulon, J. & De Bergevin, F. (1997). *J. Phys. IV*, **7**(C2), 309–313.

Varga, L., Malgrange, C., Brouder, C., Neumann, C., Rogalev, A. & Goulon, J. (1998). Unpublished.